

Learning MRI Artifact Removal With Unpaired Data

Siyuan Liu¹, Kim-Han Thung¹, Liangqiong Qu¹, Weili Lin¹, Dinggang Shen¹, Pew-Thian Yap^{1,✉}, and the UNC/UMN Baby Connectome Project Consortium

¹*Department of Radiology and Biomedical Research Imaging Center (BRIC), University of North Carolina at Chapel Hill, NC, U.S.A.*

Retrospective artifact correction (RAC) improves image quality post acquisition and enhances image usability. Recent machine learning driven techniques for RAC are predominantly based on supervised learning and therefore practical utility can be limited as data with paired artifact-free and artifact-corrupted images are typically insufficient or even non-existent. Here we show that unwanted image artifacts can be disentangled and removed from an image via an RAC neural network learned with unpaired data. This implies that our method does not require matching artifact-corrupted data to be either collected via acquisition or generated via simulation. Experimental results demonstrate that our method is remarkably effective in removing artifacts and retaining anatomical details in images with different contrasts.

Introduction

Structural magnetic resonance imaging (sMRI) captures high spatial-resolution details of brain anatomy, but is susceptible to artifacts caused for example by eye and head motions¹, especially when scanning pediatric, elderly, claustrophobic, and epileptic patients². Artifacts can result in unusable images and hence cause financial losses for imaging studies³. Motion artifact correction⁴ can be used to remove artifacts, improve image quality, and increase the amount of usable images. This is particularly important in view of the fact that the accuracy and reliability of subsequent analysis or diagnosis can be jeopardized by poor image quality.

Methods for correction of motion artifacts can be prospective or retrospective. Prospective techniques⁵⁻¹⁰ utilize either optical tracking of target markers placed on the head or continuously reacquired images from dedicated navigator scans for real-time motion prediction⁸. However, prospective methods require additional hardware and/or scanner modifications. Motion markers can cause patient discomfort and optical tracking requires expensive hardware, needs clear visibility of target markers, and may be sensitive to facial movements. Moreover, these methods typically assume quiescent periods with minimal motion and reacquire data when this condition is not met. This prolongs acquisition time without necessarily bringing substantial improvements to image quality when there is little motion.

In contrast, retrospective artifact correction (RAC)⁴ can be used to remove artifacts, im-

✉ Corresponding author: Pew-Thian Yap (ptyap@med.unc.edu)

prove image quality, and enhance image usability without requiring additional hardware, as motion estimation and correction are considered a part of the image reconstruction process. Retrospective techniques can be acquisition-based or software-based. One representative technique of acquisition-based methods is PROPELLER¹¹, which is a self-navigation technique that utilizes a number of concentric blades rotated at different angles to cover the whole k-space. The k-space center is repeatedly sampled and used as self-navigators for the estimation of rotation and translation information. It has been shown to be effective for 2D motion correction¹². However, acquisition-based methods such as PROPELLER can only estimate in-plane motion parameters, and the through-plane motion might disrupt signals across slices. Moreover, retrospective techniques often require additionally purposefully designed navigator sequences, more complicated designs, longer acquisition times, and impose additional constraints on imaging parameters (i.e., TR/TE/TI).

Software-based methods for post-acquisition RAC⁴ can be used to remove artifacts without modification of sequences, mounting of markers, and constraining acquisition parameters. They are inexpensive post-processing methods that can be readily incorporated across all scanners. Particularly, deep neural networks (DNNs), such as convolutional neural networks (CNNs), have demonstrated great potential for simultaneous removal of a variety of artifacts irrespective of the acquisition scheme^{13,14}. CNNs are typically trained in a supervised manner, which in RAC requires paired artifact-corrupted and artifact-free images. Such paired data can be collected by scanning the same subjects without and with motions, which can be impractical, costly, and time-consuming. Artifact-corrupted images can also be generated by adding simulated artifacts to artifact-free images¹⁵⁻¹⁸. However, simulations might not accurately and sufficiently reflect all possible forms of real artifacts.

In this paper, we consider the artifact removal problem as image translation from an artifact-corrupted domain to an artifact-free domain. We gain inspirations from unsupervised image translation techniques, such as UNIT¹⁹, CycleGAN²⁰, BicycleGAN²¹, and Pix2Pix²², which employ auto-encoders to learn invertible mappings between domain pairs using unpaired images. We introduce an end-to-end disentangled unsupervised cycle-consistent adversarial network (DUN-CAN), which can be trained using unpaired data for flexible and simultaneous removal of various sMRI artifacts. We employ cycle translations between artifact-corrupted and artifact-free domains, where each cycle translation is defined as a forward translation from one domain to its target domain, followed by a backward translation from the target domain to the original domain. Both the forward and backward translations are realized with auto-encoders. Note that each MR image, even deemed good in quality, may inevitably contain some artifacts. Therefore, we assume that images from either artifact-corrupted or artifact-free domains are composed of an anatomical content component, residing in a domain-invariant content space, and an artifact component, residing in a domain-specific artifact space. The auto-encoders disentangle these two components in an image via two kinds of encoders in each domain translation mapping, i.e., a content encoder, which captures anatomical structures shared across domains, and an artifact encoder, which captures artifacts specific to a domain. Then, the decoder ensembles the extracted content and artifact features from

both encoders to translate images to the target domain. To ensure complete disentanglement of content and artifact components, we propose a multi-scale content consistency (MS-CC) loss and a content-swapping mechanism supervised by adversarial learning. We also design a multi-scale reconstruction consistency (MS-RC) loss, including a pixel reconstruction consistency (PRC) loss, an edge reconstruction consistency (ERC) loss, and a structure reconstruction consistency (SRC) loss, to avoid degradation of structural details. In addition, we propose an image quality consistency (IQC) loss to ensure that no structural details are removed from artifact-free images. The architecture of DUNCAN is summarized in Figure 1 and detailed in the Methods section.

Results

Datasets We evaluated DUNCAN using (i) An in vivo dataset of T1- and T2-weighted images of children scanned from one month to six years of age²³; and (ii) An in silico dataset of T1- and T2-weighted images with simulated artifacts.

We denote the in vivo datasets for T1- and T2-weighted MR images as IV_T1 and IV_T2, respectively. For each modality, we selected 20 artifact-free and 20 artifact-corrupted volumes for training, and 10 artifact-corrupted volumes for testing. We extracted 76 to 85 axial slices from each image volume, resulting in a total of 1620, 1600, and 800 axial slices respectively from the 20 artifact-free, 20 artifact-corrupted, and 10 artifact-corrupted T1-weighted volumes for IV_T1 and 1520, 1550, and 800 axial slices respectively from the 20 artifact-free, 20 artifact-corrupted, and 10 artifact-corrupted T2-weighted volumes for IV_T2. Each artifact-corrupted image volume was labeled with one of three artifact severity levels: minor, moderate, or heavy.

To generate the in silico datasets, we synthesized artifact-corrupted images from the artifact-free images from IV_T1 and IV_T2 with three levels of artifacts, i.e., minor, moderate, and heavy. The resulting datasets are respectively denoted as IS_T1_MIN, IS_T1_MOD, and IS_T1_HVY for T1-weighted images, and IS_T2_MIN, IS_T2_MOD, and IS_T2_HVY for T2-weighted images. We simulated the motion artifacts in k-space, reflecting background noise movements, swallowing-like movements, and random sudden movements. We generated the background noise movement via a pseudorandomized series (Perlin noise²⁴) with magnitude of 5, the swallowing-like movements via multiplications with linear phase shifts in motion directions, i.e., translations along z -axis and rotations along x -axis, and the random sudden movements via sudden changes in the magnitudes of motions in all directions. For IS_T1_MIN, IS_T1_MOD, and IS_T1_HVY, 1620, 1620, 800, and 800 axial slices were extracted, respectively, from the 20 artifact-free, 20 synthesized artifact-corrupted, 10 artifact-free, and 10 synthesized artifact-corrupted T1-weighted volumes. For IS_T2_MIN, IS_T2_MOD, and IS_T2_HVY, 1520, 1520, 800, and 800 axial slices were extracted, respectively, from the 20 artifact-free, 20 synthesized artifact-corrupted, 10 artifact-free, and 10 synthesized artifact-corrupted T2-weighted volumes.

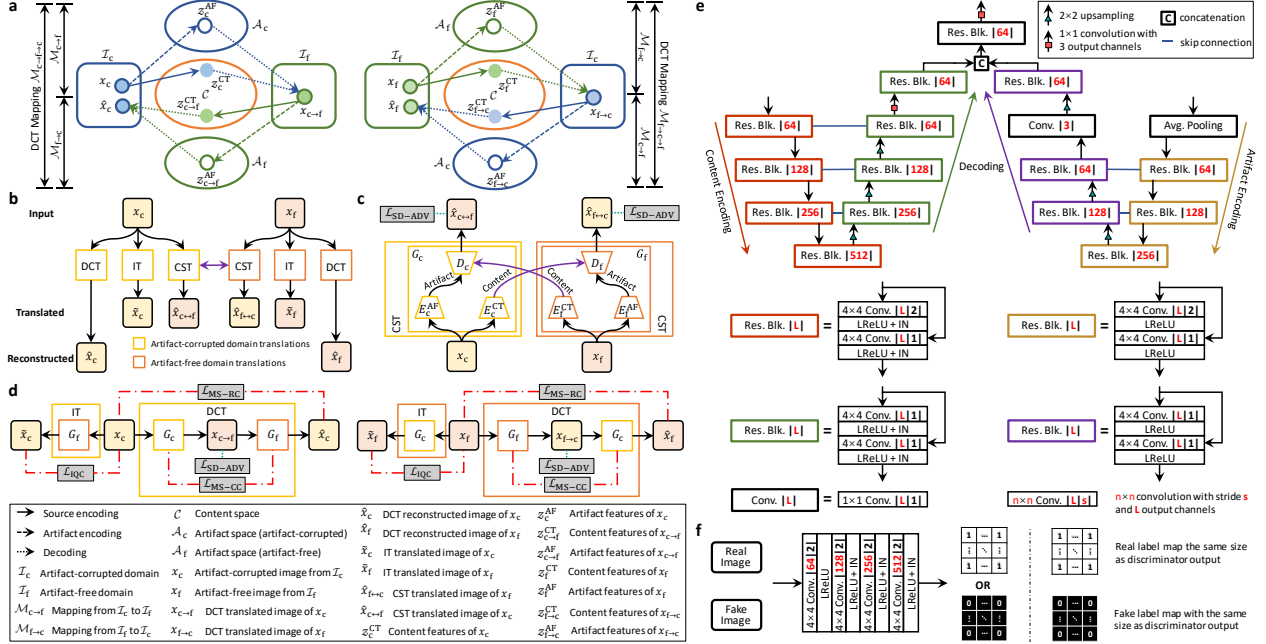


Figure 1: Overview of DUNCAN. **a**, Disentangled cycle translation (DCT) mapping $\mathcal{M}_{c \rightarrow f \rightarrow c}$ consists of two sequential domain mappings $\mathcal{M}_{c \rightarrow f}$ and $\mathcal{M}_{f \rightarrow c}$. For $\mathcal{M}_{c \rightarrow f}$, an artifact-corrupted image x_c is first encoded in the domain-invariant content space \mathcal{C} and the domain-specific artifact space \mathcal{A}_c to obtain the content (CT) information z_c^{CT} and artifact (AF) information z_c^{AF} , respectively. Then, z_c^{CT} and z_c^{AF} are decoded to remove artifacts from x_c , and to obtain the intermediate translated image $x_{c \rightarrow f}$ in the artifact-free domain \mathcal{I}_f . For $\mathcal{M}_{f \rightarrow c}$, $x_{c \rightarrow f}$ is first encoded in the content space \mathcal{C} and the artifact space \mathcal{A}_f to obtain the content information $z_{c \rightarrow f}^{CT}$ and the artifact information $z_{c \rightarrow f}^{AF}$, respectively. Then, $z_{c \rightarrow f}^{CT}$ and $z_{c \rightarrow f}^{AF}$ are decoded to add artifacts to $x_{c \rightarrow f}$ to reconstruct image \hat{x}_c . DCT mapping $\mathcal{M}_{c \rightarrow f \rightarrow c}$ is hence $\{x_c \in \mathcal{I}_c\} \rightarrow \{z_c^{CT} \in \mathcal{C}, z_c^{AF} \in \mathcal{A}_c\} \rightarrow \{x_{c \rightarrow f} \in \mathcal{I}_f\} \rightarrow \{z_{c \rightarrow f}^{CT} \in \mathcal{C}, z_{c \rightarrow f}^{AF} \in \mathcal{A}_f\} \rightarrow \{\hat{x}_c \in \mathcal{I}_c\}$. Conversely, DCT mapping $\mathcal{M}_{f \rightarrow c \rightarrow f}$ is $\{x_f \in \mathcal{I}_f\} \rightarrow \{z_f^{CT} \in \mathcal{C}, z_f^{AF} \in \mathcal{A}_f\} \rightarrow \{x_{f \rightarrow c} \in \mathcal{I}_c\} \rightarrow \{z_{f \rightarrow c}^{CT} \in \mathcal{C}, z_{f \rightarrow c}^{AF} \in \mathcal{A}_c\} \rightarrow \{\hat{x}_f \in \mathcal{I}_f\}$. **b**, DUNCAN takes any two unpaired images, i.e., one image x_c from artifact-corrupted domain \mathcal{I}_c and one image x_f from artifact-free domain \mathcal{I}_f , as inputs. The artifact-corrupted and artifact-free domain cycles incorporate the DCT mappings $\mathcal{M}_{c \rightarrow f \rightarrow c}$ and $\mathcal{M}_{f \rightarrow c \rightarrow f}$, respectively. The content-swapping translation (CST) and identity translation (IT), respectively, give the content-swapped translated images, i.e., $\tilde{x}_{f \rightarrow c}$ and $\tilde{x}_{c \rightarrow f}$, and identity translated images, i.e., \tilde{x}_c and \tilde{x}_f . **c**, CST in artifact-corrupted and artifact-free domains. **d**, DCT and IT in artifact-corrupted and artifact-free domains. **e**, Network architecture of the proposed auto-encoder (G_c or G_f). **f**, Network architecture of the discriminator. The discriminator employs a fully convolutional network (FCN) to determine if the generate image is real or fake based on a semantic map²².

Evaluation Metrics To quantitatively evaluate the performance of DUNCAN on the in silico datasets, several image quality metrics, including mean square error (MSE), structural similarity index (SSIM)²⁵, multi-scale structural similarity index (MS-SSIM)²⁶, peak signal-to-noise ratio

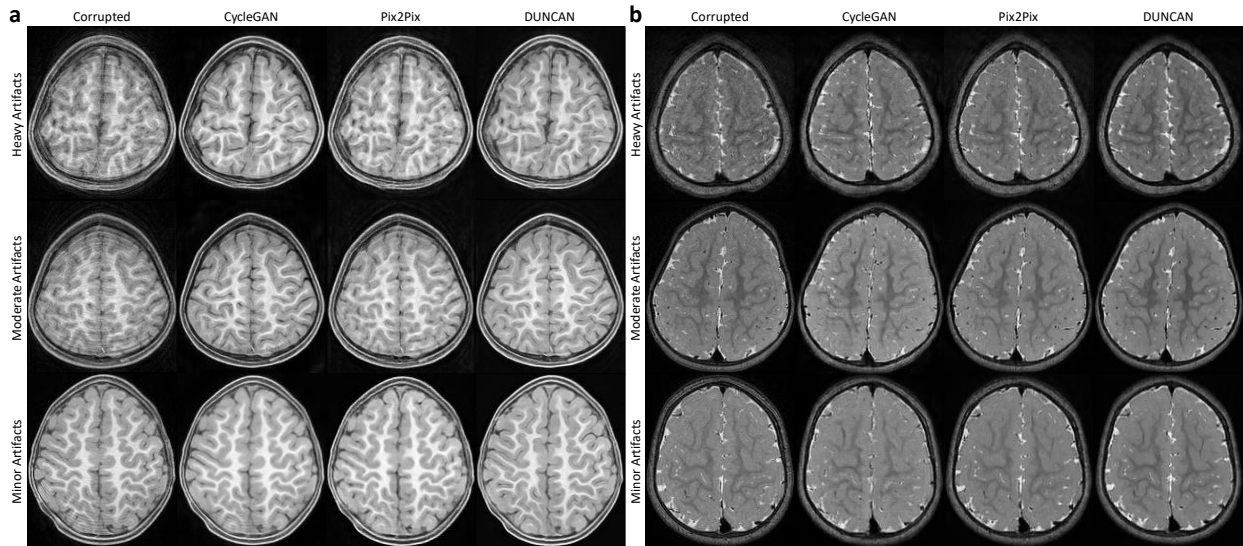


Figure 2: **Visual comparison of corrected in vivo images.** **a**, T1-weighted images and, **b**, T2-weighted images corrected using various methods. From top to bottom are images with heavy, moderate, and minor artifacts. In **a** and **b**, the original artifact-corrupted images are shown in the first column and the images corrected using CycleGAN, Pix2Pix, and DUNCAN are shown respectively in the second to fourth columns. DUNCAN outperforms the other methods in removing artifacts and in preserving anatomical details.

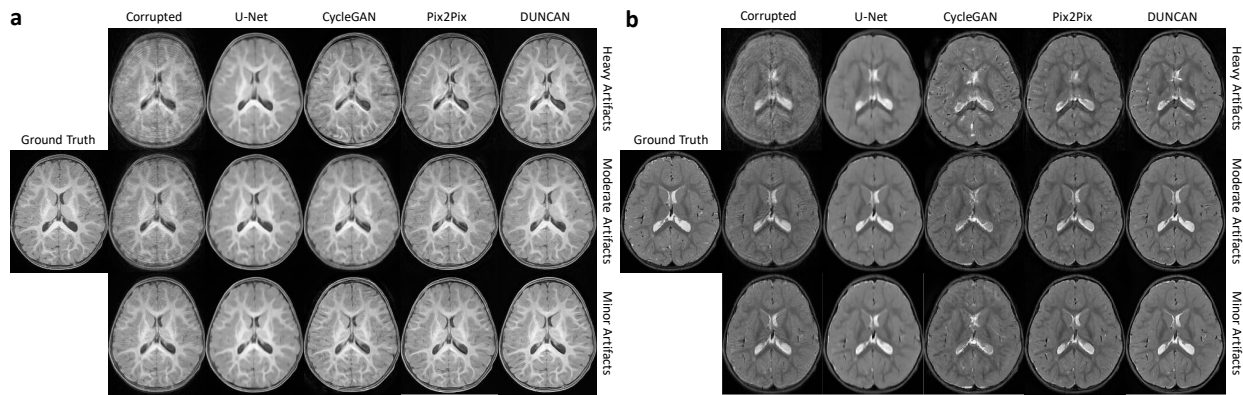


Figure 3: **Visual comparison of corrected in silico images.** **a**, T1-weighted images and, **b**, T2-weighted images corrected using various methods. From top to bottom are images with heavy, moderate, and minor artifacts. In **a** and **b**, the ground truth is shown in the first column, the original artifact-corrupted images in the second column, and the images corrected using U-Net, CycleGAN, Pix2Pix, and DUNCAN, respectively, in the third to sixth columns. DUNCAN removes more artifacts and preserves more anatomical details in agreement with the ground truth.

(PSNR), visual information fidelity (VIF)²⁷, and universal quality index (UQI)²⁸, were utilized to gauge the quality of the artifact-corrected images. We used the default settings for all the hyper-

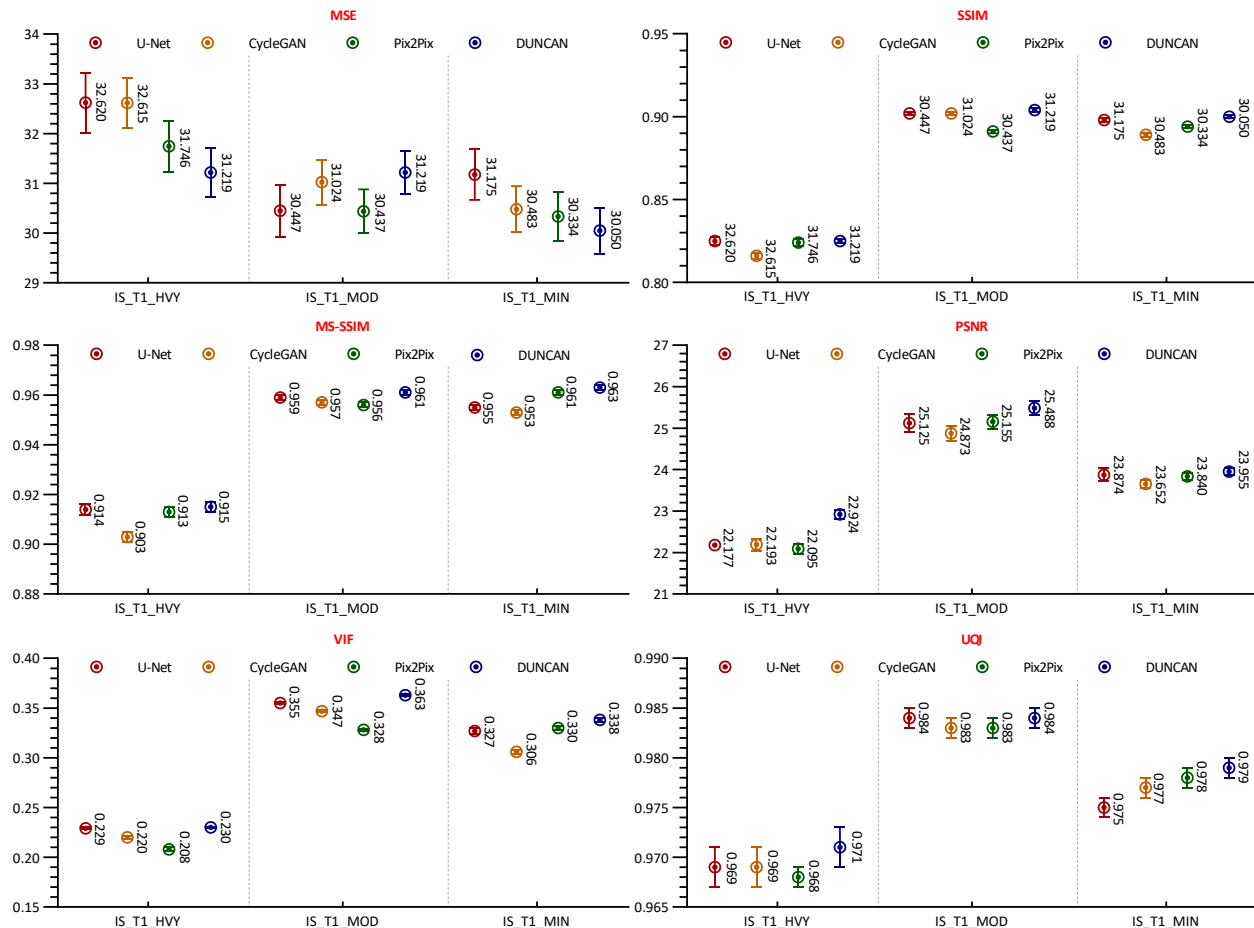


Figure 4: **Quantitative comparison of corrected in silico T1-weighted images.** Numerical evaluation conducted with different levels of artifacts (heavy, moderate, and minor) and various metrics (MSE, SSIM, MS-SSIM, PSNR, VIF, and UQI). The bars show the means and the error bars show the standard errors on the means. The sample sizes of IS_T1_HVY, IS_T1_MOD, and IS_T1_MIN are 200, 300, 300, respectively. Compared with the other methods, DUNCAN yields lower MSE and higher SSIM, MS-SSIM, PSNR, VIF, and UQI.

parameters of the evaluation metrics. For all metrics, except MSE, higher values indicate better performance.

Compared Methods To verify the effectiveness and superiority of DUNCAN, we compared it with three state-of-the-art methods that are closely related to our task, i.e., one supervised method – U-Net¹³ – and two unsupervised methods – CycleGAN²⁰ and Pix2Pix²² – implemented with Keras¹. Pix2Pix differs from CycleGAN by using a least-squares adversarial loss²⁹ and PatchGAN²² as the discriminator.

¹<https://github.com/eriklindernoren/Keras-GAN/>

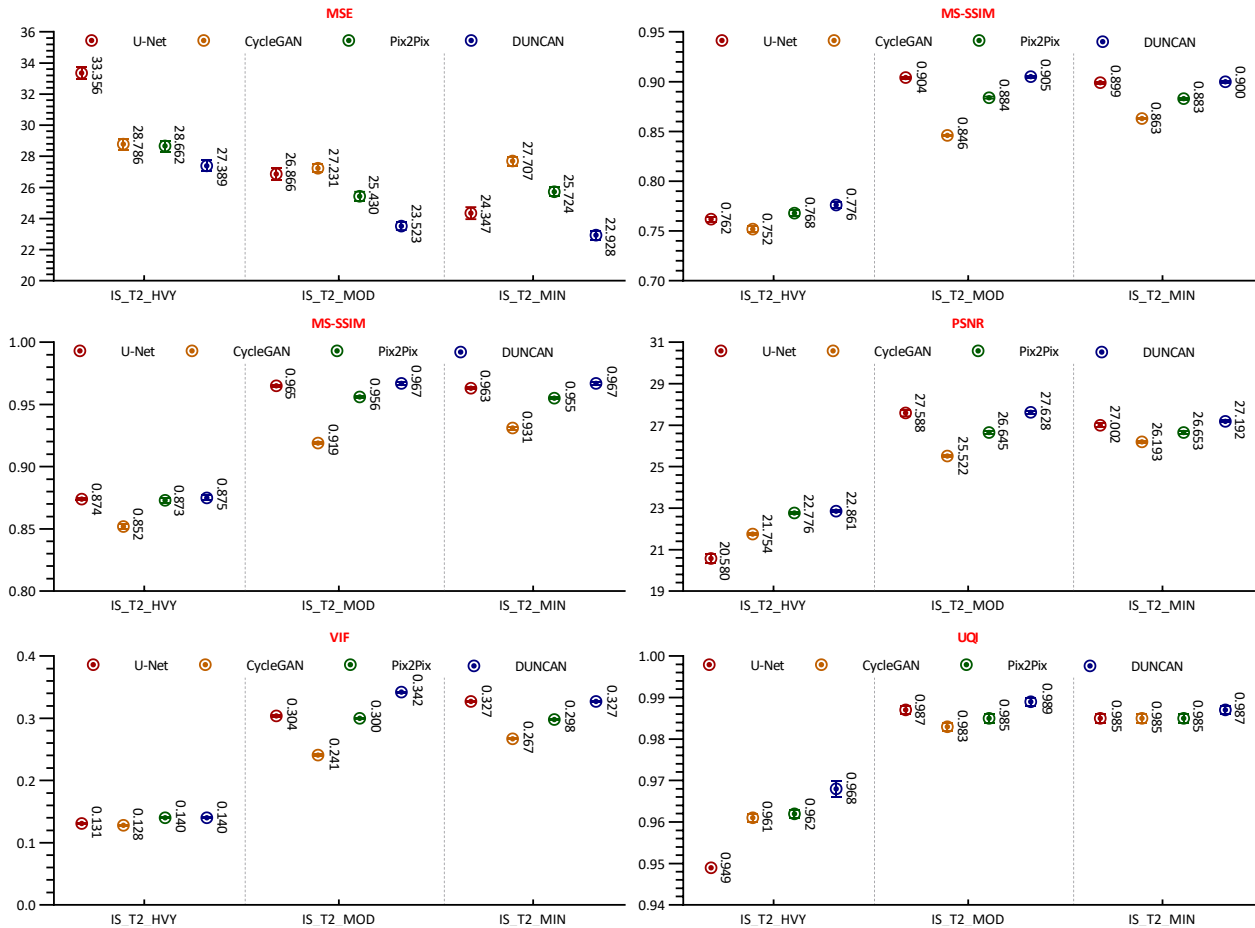


Figure 5: **Quantitative comparison of corrected in silico T2-weighted images.** Numerical evaluation conducted with different levels of artifacts (heavy, moderate, and minor) and various metrics (MSE, SSIM, MS-SSIM, PSNR, VIF, and UQI). The bars show the means and the error bars show the standard errors on the means. The sample sizes of IS_T2_HVY, IS_T2_MOD, and IS_T2_MIN are 200, 300, 300, respectively. Compared with the other methods, DUNCAN yields lower MSE and higher SSIM, MS-SSIM, PSNR, VIF, and UQI.

Performance Evaluation Using In Vivo Datasets Since no ground truth is available for the in vivo images, only qualitative comparisons were conducted. The comparison results for different levels of artifacts are shown for the T1-weighted and T2-weighted datasets in Figures 2a and 2b, respectively. CycleGAN and Pix2Pix are unable to remove the artifacts completely for different levels of artifacts in the T1- and T2-weighted images. In comparison, DUNCAN is able to remove artifacts with varying severity without introducing new artifacts.

Performance Evaluation Using In Silico Datasets Visual comparison results for the in silico T1- and T2-weighted datasets are provided in Figures 3a and 3b, respectively. The error maps, gradient maps, and gradient error maps for T1- and T2-weighted images are provided in Supplementary

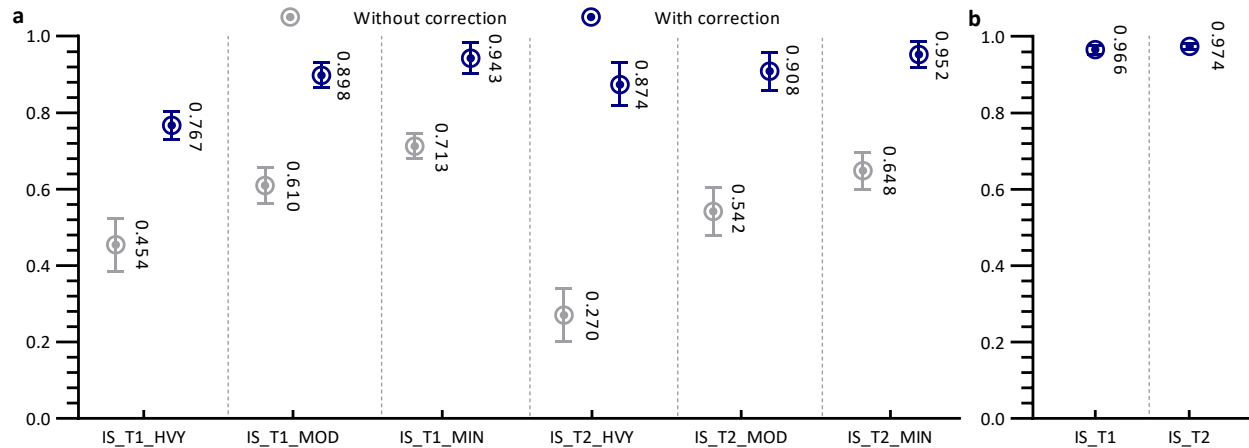


Figure 6: **Segmentation accuracy of in silico images.** **a**, DSC comparison of artifact-corrupted images with and without correction, indicating artifact removal improves image usability. **b**, Applying DUNCAN on the artifact-free images do not degrade image details, as indicated by the high DSCs. The bars show the means and the error bars show the standard errors on the means. The sample size is 10 for each case.

Figures 1–3, respectively. Quantitative comparison results using various evaluation metrics are summarized in Figures 4 and 5, respectively. Quantitative comparison results of gradient maps using various evaluation metrics on in silico T1- and T2-weighted images are included in Supplementary Figure 4. CycleGAN and Pix2Pix yield similar performance for the various evaluation metrics, but in terms of visual appearance, Pix2Pix is significantly better than CycleGAN due to its PatchGAN discriminator and least-squares adversarial loss. Although U-Net was trained with paired data and performs better than CycleGAN and Pix2Pix for the various evaluation metrics, CycleGAN and Pix2Pix generate images that are sharper than U-Net, both qualitatively and quantitatively, as illustrated in Supplementary Figures 2–4. This is due to the use of adversarial learning in CycleGAN and Pix2Pix. In comparison, as DUNCAN utilizes both adversarial learning and disentangled representation learning of artifacts and contents, it yields better performance in artifact removal and better capability in maintaining structural information in artifact-corrupted images. Even when corrupted with heavy artifacts, image details can still be satisfactorily recovered by DUNCAN.

Tissue Segmentation To further demonstrate that DUNCAN can improve image usability, we applied BET³⁰ and FAST³¹ on the testing data in IS_T1 and IS_T2 for brain extraction and tissue segmentation, respectively. We report in Figure 6 the tissue segmentation accuracy before and after artifact correction, as measured by the Dice similarity coefficient (DSC). Tissue segmentation maps from the artifact-free images were used as references. The results shown in Figure 6a indicate that DSCs are improved remarkably by DUNCAN correction. To validate the quality preservation property of DUNCAN for artifact-free images, we also evaluated the tissue segmentation accuracy

of artifact-free images processed with DUNCAN. The high DSCs shown in Figure 6b indicate that the quality of artifact-free images is preserved.

Discussion We have demonstrated that DUNCAN can be applied to MR images for post-acquisition artifact removal. DUNCAN is therefore useful when raw k-space data and reconstruction algorithms are not available. DUNCAN is a flexible method for RAC irrespective of the acquisition technique. For training, the user only needs to label the images as artifact-corrupted or artifact-free. No additional images need to be acquired and no knowledge of MR physics is needed to simulate artifacts. DUNCAN can potentially allow image imperfections such as noise, streaking, and ghosting to be removed without explicitly generating them for supervised training. DUNCAN can be incorporated in a quality control pipeline to improve image usability. We also note that DUNCAN can be used, via translation of artifact-free to artifact-corrupted images, to generate natural and realistic artifacts that can be used for supervised or unsupervised training of machine learning algorithms.

Acknowledgments This work was supported in part by National Institutes of Health grants (EB006733, AG053867, MH117943, MH104324, MH110274) and the efforts of the UNC/UMN Baby Connectome Project Consortium. The authors thank Dr. Xiaopeng Zong of the University of North Carolina at Chapel Hill for an initial discussion on motion artifact simulation and Dr. Yoonmi Hong of the University of North Carolina at Chapel Hill and Dr. Yong Chen of Case Western Reserve University for proofreading the paper.

Competing Interests The authors declare that they have no competing financial interests.

Correspondence Correspondence and requests for materials should be addressed to Pew-Thian Yap (email: ptyap@med.unc.edu).

Data Availability The data used in this paper were provided by the investigative team of the UNC/UMN Baby Connectome Project. The data can be obtained from the National Institute of Mental Health Data Archive (NDA) (<http://nda.nih.gov/>) or by contacting the investigative team²³.

Code Availability The source code and trained models for this study are publicly available on Zenodo (<https://zenodo.org/record/3742351>)³².

Author Contribution SL designed the framework and network architecture, carried out the implementation, performed the experiments, and analyzed the data. SL and PTY wrote the manuscript. SL, KHT, and PTY revised the manuscript. LQ contributed to the initial formulation of the method before moving to Stanford University. WL provided the infant data for training and testing. PTY conceived the study and were in charge of overall direction and planning. DS was involved in the initial discussion of the problem when he was with the University of North Carolina at Chapel Hill. All work was done at the University of North Carolina at Chapel Hill.

Methods

In this work, we (i) consider the artifact removal problem as image translation from an artifact-corrupted domain to an artifact-free domain; (ii) propose an end-to-end unsupervised RAC framework based on a disentangled unsupervised cycle-consistent adversarial network (DUNCAN, see Figure 1), which employs two auto-encoders to learn a cycle translation mapping that translates the images forward and backward between the artifact-corrupted and artifact-free domains; (iii) adopt two encoders to embed the images in a domain-invariant content space, which contains anatomical information, and a domain-specific artifact space, which captures artifact and noise information, and adopt a decoder to translate the images to a target domain using the encoded content and artifact features; (iv) realize content-artifact disentanglement, hinging on determining the domain-invariant content space using two strategies: a multi-scale content consistency (MS-CC) loss to keep content features consistent across domains and a content-swapping mechanism to ensure the domain-invariance of the content space; and (v) introduce a quality preservation mechanism to ensure that no image details are removed.

Disentangled Cycle Translation Mapping Let \mathcal{I}_c and \mathcal{I}_f be the domains of artifact-corrupted and artifact-free MR images, respectively. Our method aims to learn the nonlinear mappings between the two domains, i.e., $\mathcal{M}_{c \rightarrow f} : \mathcal{I}_c \rightarrow \mathcal{I}_f$ and $\mathcal{M}_{f \rightarrow c} : \mathcal{I}_f \rightarrow \mathcal{I}_c$, using unpaired training images. In practice, each acquired MR image, even with good quality, may inevitably contain artifacts. Therefore, we assume that each MR image is a nonlinear combination of content and artifact components. For two unpaired images ($x_c \in \mathcal{I}_c, x_f \in \mathcal{I}_f$), disentangled cycle translation (DCT) mapping $\mathcal{M}_{c \rightarrow f \rightarrow c} : \mathcal{I}_c \rightarrow \mathcal{I}_f \rightarrow \mathcal{I}_c$ is accomplished with sequential forward and backward translation mappings $\mathcal{M}_{c \rightarrow f}$ and $\mathcal{M}_{f \rightarrow c}$; conversely, the DCT mapping $\mathcal{M}_{f \rightarrow c \rightarrow f} : \mathcal{I}_f \rightarrow \mathcal{I}_c \rightarrow \mathcal{I}_f$ is realized with $\mathcal{M}_{f \rightarrow c}$ and $\mathcal{M}_{c \rightarrow f}$, as illustrated in Figure 1a. Specifically, taking DCT mapping $\mathcal{M}_{c \rightarrow f \rightarrow c}$ as an example, for forward translation mapping $\mathcal{M}_{c \rightarrow f}$, we first encode x_c in two latent spaces, i.e., the domain-invariant content space \mathcal{C} and the domain-specific artifact space \mathcal{A}_c , to obtain two disentangled representations, i.e., the artifact (AF) representation z_c^{AF} and the content (CT) representation z_c^{CT} , respectively. We then build a decoder based on the disentangled representations to construct intermediate image $x_{c \rightarrow f}$ in the artifact-free domain \mathcal{I}_f . The forward translation mapping $\mathcal{M}_{c \rightarrow f}$ for x_c can be summarized as $\{x_c \in \mathcal{I}_c\} \rightarrow \{z_c^{\text{CT}} \in \mathcal{C}, z_c^{\text{AF}} \in \mathcal{A}_c\} \rightarrow \{x_{c \rightarrow f} \in \mathcal{I}_f\}$. We then further conduct a backward translation mapping $\mathcal{M}_{f \rightarrow c}$ on $x_{c \rightarrow f}$. We first encode $x_{c \rightarrow f}$ as $z_{c \rightarrow f}^{\text{CT}}$ in content space \mathcal{C} and $z_{c \rightarrow f}^{\text{AF}}$ in artifact space \mathcal{A}_f . Note that this artifact space is specific to input from domain \mathcal{I}_f , whereas \mathcal{A}_c is specific to input from domain \mathcal{I}_c , as images from both domains have different types of artifacts manifesting in different styles. Feeding $z_{c \rightarrow f}^{\text{CT}}$ and $z_{c \rightarrow f}^{\text{AF}}$ as input to a decoder, we obtain the reconstructed artifact-corrupted image \hat{x}_c . The backward translation mapping $\mathcal{M}_{f \rightarrow c}$ for $x_{c \rightarrow f}$ can be summarized as $\{x_{c \rightarrow f} \in \mathcal{I}_f\} \rightarrow \{z_{c \rightarrow f}^{\text{CT}} \in \mathcal{C}, z_{c \rightarrow f}^{\text{AF}} \in \mathcal{A}_f\} \rightarrow \{\hat{x}_c \in \mathcal{I}_c\}$. Similarly, we also perform DCT mapping for x_f via $\mathcal{M}_{f \rightarrow c}$ and $\mathcal{M}_{c \rightarrow f}$ to obtain in sequence the intermediate artifact-corrupted image $x_{f \rightarrow c}$ and artifact-free image \hat{x}_f , i.e., $\{x_f \in \mathcal{I}_f\} \rightarrow \{z_f^{\text{CT}} \in \mathcal{C}, z_f^{\text{AF}} \in \mathcal{A}_f\} \rightarrow \{x_{f \rightarrow c} \in \mathcal{I}_c\} \rightarrow \{z_{f \rightarrow c}^{\text{CT}} \in \mathcal{C}, z_{f \rightarrow c}^{\text{AF}} \in \mathcal{A}_c\} \rightarrow \{\hat{x}_f \in \mathcal{I}_f\}$.

The DUNCAN Architecture Figure 1b shows an overview of the network architecture of DUNCAN, consisting of two DCT mappings (artifact-corrupted and artifact-free domain cycles), two

content-swapping and identity translations (in both artifact-corrupted and artifact-free domains), and four adversarial constraints (for the generated artifact-corrupted and artifact-free images). As described in the previous section, the artifact-corrupted and artifact-free domain cycles aim to perform DCT mappings $\mathcal{M}_{c \rightarrow f \rightarrow c}$ and $\mathcal{M}_{f \rightarrow c \rightarrow f}$, respectively, using two domain translation mappings, i.e., $\mathcal{M}_{f \rightarrow c}$ and $\mathcal{M}_{c \rightarrow f}$. Each domain translation mapping is realized by two encoders to disentangle an image into content and artifact features, and one decoder to reconstruct the target-domain image using the disentangled features, as illustrated in Figure 1c. More specifically, the mapping $\mathcal{M}_{f \rightarrow c}$ is realized by content encoder E_f^{CT} , artifact encoder E_f^{AF} , and decoder D_f , whereas the mapping $\mathcal{M}_{c \rightarrow f}$ is realized by content encoder E_c^{CT} , artifact encoder E_c^{AF} , and decoder D_c . With any two unpaired images $x_c \in \mathcal{I}_c$ and $x_f \in \mathcal{I}_f$ as inputs, the encoders and decoders are learned to respectively reconstruct images \hat{x}_c and \hat{x}_f via DCT mappings $\mathcal{M}_{c \rightarrow f \rightarrow c}$ and $\mathcal{M}_{f \rightarrow c \rightarrow f}$.

Using the domain-invariant property of the content space, we propose content-swapping translation (CST) for complete representation disentanglement, as illustrated in Figure 1c. The idea behind this mechanism is that when the content and artifact information are completely disentangled, swapping the domain-invariant content information between domain translations should not lead to changes in translation outcomes. Specifically, we replace content information from $E_c^{\text{CT}}(x_c)$ in domain translation $\mathcal{M}_{c \rightarrow f}$ with content information from $E_f^{\text{CT}}(x_f)$ to construct content-swapped translated image $\hat{x}_{c \leftrightarrow f} \in \mathcal{I}_f$ via decoder D_c . Similarly, we replace content information from $E_f^{\text{CT}}(x_f)$ in domain translation $\mathcal{M}_{f \rightarrow c}$ with content information from $E_c^{\text{CT}}(x_c)$ to generate content-swapped translated image $\hat{x}_{f \leftrightarrow c} \in \mathcal{I}_c$ via decoder D_f . The translated images $\hat{x}_{c \leftrightarrow f}$ and $\hat{x}_{f \leftrightarrow c}$, respectively, are constrained by x_f and x_c via discriminators $D_{c \leftrightarrow f}^{\text{ADV}}$ and $D_{f \leftrightarrow c}^{\text{ADV}}$.

Furthermore, we constrain the forward translation mappings with identity translation (IT) mappings, as illustrated in Figure 1d, to maintain image quality when no alteration is expected. Specifically, when translation mappings $\mathcal{M}_{c \rightarrow f}$ and $\mathcal{M}_{f \rightarrow c}$ are applied to x_f and x_c , respectively, the mappings are constrained to result in identity reconstructions $\tilde{x}_f \in \mathcal{I}_f$ and $\tilde{x}_c \in \mathcal{I}_c$. A set of consistency losses are used to ensure that the identity translated images are consistent with the corresponding input images.

Auto-Encoder Architecture We devise two auto-encoders G_c and G_f to respectively generate artifact-free and artifact-corrupted images. Each auto-encoder, with architecture illustrated in Figure 1e, consists of (i) a content encoder, E_c^{CT} or E_f^{CT} , and an artifact encoder, E_c^{AF} or E_f^{AF} , that respectively map an input image to the domain-invariant latent space \mathcal{C} and the domain-specific latent space, \mathcal{A}_c or \mathcal{A}_f , to respectively extract the content and artifact information of the image, and (ii) a decoder, D_c or D_f , that generates from the extracted features an image in the target domain of the auto-encoder. We describe next the details for each component of the auto-encoder.

Content Encoder The content encoder takes the original image as input, and extracts content features through 4 residual blocks. Each residual block consists of 4×4 convolution, leaky ReLU, and instance normalization (IN)³³ layers. We use an IN layer instead of a batch normalization layer³³ to accelerate model convergence and maintain independence between features. All normalized feature maps are activated by leaky ReLU with negative slope 0.2.

Artifact Encoder We first down-sample the input image using 2×2 average-pooling in the artifact encoder. Then, we extract features from the down-sampled image using 3 residual blocks without IN layers since IN removes the feature means and variances, which contain important artifact information.

Decoder The decoder takes the extracted content and artifact features as input and generates, using a set of up-sampling layers and residual blocks, a content image and an artifact image, which are concatenated and then fused through a residual block and an 1×1 convolution layer to generate the translated image.

Adversarial Learning We employ generative adversarial networks (GANs) to better learn the translation mappings between the artifact-free and artifact-corrupted image domains. A GAN is comprised of a generator network and a discriminator network. In our case, the auto-encoder acts as the generator network by translating an input image to a target-domain image. The discriminator network is a classifier that distinguishes between real and fake images. As training progresses, the generator is getting better at fooling the discriminator, and the discriminator is getting better at distinguishing real and fake images. We employ two discriminators D_c^{ADV} and $D_{f \rightarrow c}^{\text{ADV}}$ in the artifact-corrupted domain and another two discriminators D_f^{ADV} and $D_{c \rightarrow f}^{\text{ADV}}$ in the artifact-free domain. We use PatchGAN²², shown in Figure 1f, as the discriminators. The numbers of filters are 64, 128, 256, 512 for the convolution layers and the number of output channel is 1. Leaky ReLU activation is implemented with a negative slope coefficient of 0.2.

Disentangled Representation Learning We took several measures to ensure that our encoders can properly disentangle content and artifact information from an input image. First, as content space \mathcal{C} is domain-invariant, i.e., shared between the artifact-free and artifact-corrupted domains, the content information of an image and its generated counterpart in the target domain should be consistent. For example, the content information of x_c and $x_{c \rightarrow f}$ should be consistent, and so should x_f and $x_{f \rightarrow c}$. To this end, we propose a multi-scale content consistency (MS-CC) loss based on the low- and high-level features of the content encoders to respectively encourage the consistency of structural and semantic content information. Second, discriminating between real and content-swapped generated images via discriminators $D_{f \rightarrow c}^{\text{ADV}}$ and $D_{c \rightarrow f}^{\text{ADV}}$ also ensures better disentanglement by the encoders.

Image Quality Consistency (IQC) To ensure that the image quality of an input image is similar to the translated image, we propose a pixel-wise image quality consistency (IQC) loss to encourage the auto-encoders in the translation mappings $\mathcal{M}_{f \rightarrow c}$ and $\mathcal{M}_{c \rightarrow f}$ to perform as identity translation mappings $\mathcal{M}_{c \rightarrow c} : \mathcal{I}_c \rightarrow \mathcal{I}_c$ and $\mathcal{M}_{f \rightarrow f} : \mathcal{I}_f \rightarrow \mathcal{I}_f$ when respectively given artifact-corrupted and artifact-free images. The IQC loss encourages the artifact-free image generator to not remove image details when given a good quality image. Similarly, the IQC loss encourages the artifact-corrupted image generator to not introduce any additional artifacts when given an artifact-corrupted image.

Loss Functions We leverage two types of loss functions, i.e., consistency losses and adversarial losses to facilitate model training, as illustrated in Figures 1c and 1d.

Consistency Losses We utilize three consistency losses: multi-scale content consistency (MS-CC) loss $\mathcal{L}_{\text{MS-CC}}$, which measures content consistency between the input and output of the forward translation of each DCT (i.e., $\mathcal{M}_{c \rightarrow f}$ in $\mathcal{M}_{c \rightarrow f \rightarrow c}$ and $\mathcal{M}_{f \rightarrow c}$ in $\mathcal{M}_{f \rightarrow c \rightarrow f}$), multi-scale reconstruction consistency (MS-RC) loss $\mathcal{L}_{\text{MS-RC}}$, which computes the reconstruction consistency between an image and its reconstructed counterpart in the same domain, and image quality consistency (IQC) loss, which computes the image quality consistency between an image and its identity translated counterpart in the same domain.

The MS-CC loss measures low- and high-level content feature differences and is formulated as

$$\mathcal{L}_{\text{MS-CC}} = \sum_i [\mathbb{E}_{x_c \sim \mathcal{I}_c} \|\phi_c^i(x_c) - \phi_f^i(x_{c \rightarrow f})\|_1 + \mathbb{E}_{x_f \sim \mathcal{I}_f} \|\phi_f^i(x_f) - \phi_c^i(x_{f \rightarrow c})\|_1], \quad (1)$$

where x_c and x_f denote the artifact-corrupted and artifact-free images, respectively, and $x_{c \rightarrow f} = D_c(z_c^{\text{CT}}, z_c^{\text{AF}})$ and $x_{f \rightarrow c} = D_f(z_f^{\text{CT}}, z_f^{\text{AF}})$ denote the corresponding artifact-free and artifact-corrupted images generated by the decoders, respectively. $\phi_c^i(\cdot)$ and $\phi_f^i(\cdot)$ denote the outputs of the i -th residual block of the content encoders E_c^{CT} and E_f^{CT} , respectively. $z_c^{\text{CT}} = E_c^{\text{CT}}(x_c) \in \mathcal{S}$ and $z_f^{\text{CT}} = E_f^{\text{CT}}(x_f) \in \mathcal{S}$ denote the content information extracted respectively from x_c and x_f , whereas $z_c^{\text{AF}} = E_c^{\text{AF}}(x_c) \in \mathcal{A}_c$ and $z_f^{\text{AF}} = E_f^{\text{AF}}(x_f) \in \mathcal{A}_f$ denote the artifact information extracted respectively from x_c and x_f .

We compute the MS-RC loss by combining three reconstruction consistency losses, i.e., the pixel reconstruction consistency (PRC) loss \mathcal{L}_{PRC} , the edge reconstruction consistency (ERC) loss \mathcal{L}_{ERC} , and the structure reconstruction consistency (SRC) loss \mathcal{L}_{SRC} , as defined below:

$$\mathcal{L}_{\text{MS-RC}} = \mathcal{L}_{\text{PRC}} + \mathcal{L}_{\text{ERC}} + \mathcal{L}_{\text{SRC}}, \quad (2)$$

$$\mathcal{L}_{\text{PRC}} = \mathbb{E}_{x_c \sim \mathcal{I}_c} \|x_c - \hat{x}_c\|_1 + \mathbb{E}_{x_f \sim \mathcal{I}_f} \|x_f - \hat{x}_f\|_1, \quad (3)$$

$$\mathcal{L}_{\text{ERC}} = \mathbb{E}_{x_c \sim \mathcal{I}_c} \|\psi_L(x_c) - \psi_L(\hat{x}_c)\|_1 + \mathbb{E}_{x_f \sim \mathcal{I}_f} \|\psi_L(x_f) - \psi_L(\hat{x}_f)\|_1, \quad (4)$$

$$\mathcal{L}_{\text{SRC}} = \mathbb{E}_{x_c \sim \mathcal{I}_c} \|\psi_H(x_c) - \psi_H(\hat{x}_c)\|_1 + \mathbb{E}_{x_f \sim \mathcal{I}_f} \|\psi_H(x_f) - \psi_H(\hat{x}_f)\|_1, \quad (5)$$

where $\hat{x}_c = D_f(E_f^{\text{CT}}(x_{c \rightarrow f}), E_f^{\text{AF}}(x_{c \rightarrow f}))$ and $\hat{x}_f = D_c(E_c^{\text{CT}}(x_{f \rightarrow c}), E_c^{\text{AF}}(x_{f \rightarrow c}))$ are, respectively, the reconstructed images in the artifact-corrupted and artifact-free domains, and $\psi_L(\cdot)$ and $\psi_H(\cdot)$ are, respectively, the low-level structural information that reflects edges and high-level semantic information that reflects contents measured by a pre-trained network (i.e., VGG19³⁴ trained on ImageNet).

To preserve image quality after translation when no alteration is expected, an image quality consistency (IQC) loss is devised to measure the pixel-wise difference between the input and identity mapped images as

$$\mathcal{L}_{\text{IQC}} = \mathbb{E}_{x_c \sim \mathcal{I}_c} \|x_c - \tilde{x}_c\|_1 + \mathbb{E}_{x_f \sim \mathcal{I}_f} \|x_f - \tilde{x}_f\|_1, \quad (6)$$

where $\tilde{x}_c = D_f(E_f^{\text{CT}}(x_c), E_f^{\text{AF}}(x_c))$ and $\tilde{x}_f = D_c(E_c^{\text{CT}}(x_f), E_c^{\text{AF}}(x_f))$ are the identity mapped images of x_c and x_f , respectively.

Adversarial Losses We apply two types of adversarial losses, i.e., single-domain adversarial (SD-ADV) loss and cross-domain adversarial (CD-ADV) loss, to enhance the judgment accuracy of the discriminators. All adversarial losses are designed with the mean square error function. The SD-ADV loss is calculated in a specific domain, i.e., \mathcal{I}_c or \mathcal{I}_f , as

$$\begin{aligned} \mathcal{L}_{\text{SD-ADV}} = & \frac{1}{2} \mathbb{E}_{x_c \sim \mathcal{I}_c} (D_c^{\text{ADV}}(x_c) - I)^2 + \frac{1}{2} \mathbb{E}_{x_f \sim \mathcal{I}_f} (D_c^{\text{ADV}}(x_{f \rightarrow c}))^2 \\ & + \frac{1}{2} \mathbb{E}_{x_f \sim \mathcal{I}_f} (D_f^{\text{ADV}}(x_f) - I)^2 + \frac{1}{2} \mathbb{E}_{x_c \sim \mathcal{I}_c} (D_f^{\text{ADV}}(x_{c \rightarrow f}))^2, \end{aligned} \quad (7)$$

where D_c^{ADV} and D_f^{ADV} are the discriminators used to distinguish between real and fake images respectively in domains \mathcal{I}_c and \mathcal{I}_f , I is a matrix of ones with size $N_1 \times N_2$ matching the output of the discriminator. The cross-domain adversarial (CD-ADV) loss is defined as

$$\begin{aligned} \mathcal{L}_{\text{CD-ADV}} = & \frac{1}{2} \mathbb{E}_{x_c \sim \mathcal{I}_c} (D_{f \leftrightarrow c}^{\text{ADV}}(x_c) - I)^2 + \frac{1}{2} \mathbb{E}_{x_f \sim \mathcal{I}_f, x_c \sim \mathcal{I}_c} (D_{f \leftrightarrow c}^{\text{ADV}}(\hat{x}_{f \leftrightarrow c}))^2 \\ & + \frac{1}{2} \mathbb{E}_{x_f \sim \mathcal{I}_f} (D_{c \leftrightarrow f}^{\text{ADV}}(x_f) - I)^2 + \frac{1}{2} \mathbb{E}_{x_c \sim \mathcal{I}_c, x_f \sim \mathcal{I}_f} (D_{c \leftrightarrow f}^{\text{ADV}}(\hat{x}_{c \leftrightarrow f}))^2, \end{aligned} \quad (8)$$

where $\hat{x}_{c \leftrightarrow f} = D_c(z_f^{\text{CT}}, z_c^{\text{AF}})$ and $\hat{x}_{f \leftrightarrow c} = D_f(z_c^{\text{CT}}, z_f^{\text{AF}})$ are the images reconstructed by cross-domain content information, i.e., z_f^{CT} or z_c^{CT} , and current-domain artifact information, i.e., z_c^{AF} or z_f^{AF} .

Total Loss In summary, the total loss function of DUNCAN is

$$\mathcal{L}_{\text{total}} = \mathcal{L}_{\text{SD-ADV}} + \mathcal{L}_{\text{CD-ADV}} + \lambda_{\text{MS-CC}} \mathcal{L}_{\text{MS-CC}} + \lambda_{\text{PRC}} \mathcal{L}_{\text{PRC}} + \lambda_{\text{ERC}} \mathcal{L}_{\text{ERC}} + \lambda_{\text{SRC}} \mathcal{L}_{\text{SRC}} + \lambda_{\text{IQC}} \mathcal{L}_{\text{IQC}}, \quad (9)$$

where $\lambda_{\text{MS-CC}}$, λ_{PRC} , λ_{ERC} , λ_{SRC} , and λ_{IQC} are the loss weights used for controlling the contributions of the terms in term in Equation (9).

Implementation Details DUNCAN was implemented using Keras with Tensorflow backend. Evaluation was based on a machine with a CPU (Intel i7-8700K) and a GPU (NVIDIA GeForce GTX 1080Ti 11GB RAM). The Adam optimizer with 1×10^{-4} learning rate was utilized for minimizing the loss function. For in vivo T1- and T2-weighted datasets, i.e., IV_T1 and IV_T2, we used $\lambda_{\text{MS-CC}} = 5$, $\lambda_{\text{PCC}} = 10$, $\lambda_{\text{ERC}} = 5$, $\lambda_{\text{SRC}} = 5$, and $\lambda_{\text{IQC}} = 1$ for MS-CC, PRC, ERC, SRC, and IQC losses, respectively. For in silico T1- and T2-weighted datasets, i.e., IS_T1 and IS_T2, we used $\lambda_{\text{MS-CC}} = 10$, $\lambda_{\text{PCC}} = 20$, $\lambda_{\text{ERC}} = 10$, $\lambda_{\text{SRC}} = 10$, and $\lambda_{\text{IQC}} = 5$ for MS-CC, PRC, ERC, SRC, and IQC losses, respectively. For both the in vivo and in silico datasets, every three adjacent slices in each volume were inserted into RGB channels of a color image, which was then normalized to have a range between -1 and 1 and cropped to 208×256 from the geometric center. During training, one artifact-corrupted image and one artifact-free image were randomly selected each time as inputs.

References

1. Budde, J., Shajan, G., Scheffler, K. & Pohmann, R. Ultra-high resolution imaging of the human brain using acquisition-weighted imaging at 9.4t. *NeuroImage* **86**, 592–598 (2014).
2. Zhuo, J. & Gullapalli, R. P. MR artifacts, safety, and quality control. *RadioGraphics* **26**, 275–297 (2006).
3. Andre, J. *et al.* Toward quantifying the prevalence, severity, and cost associated with patient motion during clinical MR examinations. *J. Am. Coll. Radiol.* **12**, 689–695 (2015).
4. Zaitsev, M., Maclaren, J. & Herbst, M. Motion artifacts in MRI: A complex problem with many partial solutions. *Journal of Magnetic Resonance Imaging* **42**, 887–901 (2015).
5. Zaitsev, M., Dold, C., Sakas, G., Hennig, J. & Speck, O. Magnetic resonance imaging of freely moving objects: prospective real-time motion correction using an external optical motion tracking system. *NeuroImage* **31**, 1038–1050 (2006).
6. Qin, L. *et al.* Prospective head-movement correction for high-resolution MRI using an in-bore optical tracking system. *Magnetic Resonance in Medicine* **62**, 924–934 (2009).
7. Ooi, M. B., Krueger, S., Thomas, W. J., Swaminathan, S. V. & Brown, T. R. Prospective real-time correction for arbitrary head motion using active markers. *Magnetic Resonance in Medicine* **62**, 943–954 (2009).
8. Schulz, J. *et al.* An embedded optical tracking system for motion-corrected magnetic resonance imaging at 7T. *Magnetic Resonance Materials in Physics, Biology and Medicine* **25**, 443–453 (2012).
9. Maclaren, J. *et al.* Measurement and correction of microscopic head motion during magnetic resonance imaging of the brain. *PLoS ONE* **7**, e48088 (2012).
10. Maclaren, J., Herbst, M., Speck, O. & Zaitsev, M. Prospective motion correction in brain imaging: A review. *Magnetic Resonance in Medicine* **69**, 621–636 (2012).
11. Pipe, J. G. Motion correction with propeller mri: Application to head motion and free-breathing cardiac imaging. *Magnetic Resonance in Medicine* **42**, 963–969 (1999).
12. Vertinsky, A. T. *et al.* Performance of PROPELLER relative to standard FSE t2-weighted imaging in pediatric brain MRI. *Pediatric Radiology* **39**, 1038–1047 (2009).
13. Jin, K. H., McCann, M. T., Froustey, E. & Unser, M. Deep convolutional neural network for inverse problems in imaging. *IEEE Transactions on Image Processing* **26**, 4509–4522 (2017).
14. Haskell, M. W. *et al.* Network accelerated motion estimation and reduction (NAMER): Convolutional neural network guided retrospective motion correction using a separable motion model. *Magnetic Resonance in Medicine* **82**, 1452–1461 (2019).

15. Johnson, P. M. & Drangova, M. Motion correction in mri using deep learning. In *Proceeding of the 26th Annual Meeting ISMRM* (Paris, France, 2018).
16. Tamada, D., Kromrey, M.-L., Ichikawa, S., Onishi, H. & Motosugi, U. Motion artifact reduction using a convolutional neural network for dynamic contrast enhanced MR imaging of the liver. *Magnetic Resonance in Medical Sciences* (2019).
17. Küstner, T. *et al.* Retrospective correction of motion-affected MR images using deep learning frameworks. *Magnetic Resonance in Medicine* **82**, 1527–1540 (2019).
18. Johnson, P. M. & Drangova, M. Conditional generative adversarial network for 3d rigid-body motion correction in MRI. *Magnetic Resonance in Medicine* **82**, 901–910 (2019).
19. Liu, M.-Y., Breuel, T. & Kautz, J. Unsupervised image-to-image translation networks. In *Proceedings of Advances in Neural Information Processing Systems (NIPS)*, 700–708 (2017).
20. Zhu, J.-Y., Park, T., Isola, P. & Efros, A. A. Unpaired image-to-image translation using cycle-consistent adversarial networks. In *Proceedings of IEEE International Conference on Computer Vision (ICCV)*, 2223–2232 (2017).
21. Zhu, J.-Y. *et al.* Toward multimodal image-to-image translation. In *Advances in Neural Information Processing Systems (NIPS)*, 465–476 (2017).
22. Isola, P., Zhu, J.-Y., Zhou, T. & Efros, A. A. Image-to-image translation with conditional adversarial networks. In *Proceedings of IEEE Conference on Computer Vision and Pattern Recognition (CVPR)*, 1125–1134 (2017).
23. Howell, B. R. *et al.* The UNC/UMN baby connectome project (BCP): An overview of the study design and protocol development. *NeuroImage* **185**, 891–905 (2019).
24. Perlin, K. An image synthesizer. *ACM SIGGRAPH Computer Graphics* **19**, 287–296 (1985).
25. Wang, Z., Bovik, A., Sheikh, H. & Simoncelli, E. Image quality assessment: From error visibility to structural similarity. *IEEE Transactions on Image Processing* **13**, 600–612 (2004).
26. Wang, Z., Simoncelli, E. & Bovik, A. Multiscale structural similarity for image quality assessment. In *Proceedings of IEEE Asilomar Conference on Signals, Systems and Computers*, 1398–1402 (2003).
27. Sheikh, H. & Bovik, A. Image information and visual quality. *IEEE Transactions on Image Processing* **15**, 430–444 (2006).
28. Wang, Z. & Bovik, A. A universal image quality index. *IEEE Signal Processing Letters* **9**, 81–84 (2002).
29. Mao, X. *et al.* Least squares generative adversarial networks. In *Proceedings of IEEE International Conference on Computer Vision (ICCV)*, 2794–2802 (2017).

30. Smith, S. M. Fast robust automated brain extraction. *Human Brain Mapping* **17**, 143–155 (2002).
31. Zhang, Y., Brady, M. & Smith, S. Segmentation of brain MR images through a hidden markov random field model and the expectation-maximization algorithm. *IEEE Transactions on Medical Imaging* **20**, 45–57 (2001).
32. Liu, S. *et al.* Code used in article “Learning MRI artifact removal with unpaired data”. (2020). DOI: 10.5281/zenodo.3742351.
33. Ulyanov, D., Vedaldi, A. & Lempitsky, V. Improved texture networks: maximizing quality and diversity in feed-forward stylization and texture synthesis. In *Proceedings of IEEE Conference on Computer Vision and Pattern Recognition (CVPR)*, 6924–6932 (2017).
34. Simonyan, K. & Zisserman, A. Very deep convolutional networks for large-scale image recognition. In *Proceedings of International Conference on Learning Representations (ICLR)* (2015).